

# The magnetic field and accretion regime of CI Tau

J.-F. Donati<sup>1</sup>★, J. Bouvier<sup>2</sup>, S.H. Alencar<sup>3</sup>, C. Moutou<sup>1</sup>, L. Malo<sup>4</sup>, M. Takami<sup>5</sup>,  
F. Ménard<sup>2</sup>, C. Dougados<sup>2</sup>, G.A. Hussain<sup>7</sup> and the MaTYSSE collaboration

<sup>1</sup> *Univ. de Toulouse, CNRS, IRAP, 14 avenue Belin, 31400 Toulouse, France*

<sup>2</sup> *Univ. Grenoble Alpes, CNRS, IPAG, 38000 Grenoble, France*

<sup>3</sup> *Departamento de Física – ICEx – UFMG, Av. Antônio Carlos, 6627, 30270-901 Belo Horizonte, MG, Brazil*

<sup>4</sup> *Département de physique, Université de Montréal, C.P. 6128, Succursale Centre-Ville, Montréal, QC, Canada H3C 3J7*

<sup>5</sup> *Institute of Astronomy and Astrophysics, Academia Sinica, PO Box 23-141, 106, Taipei, Taiwan*

<sup>6</sup> *ESO, Karl-Schwarzschild-Str. 2, D-85748 Garching, Germany*

Submitted 2019 xxx – Accepted 2019 xxx

## ABSTRACT

This paper exploits spectropolarimetric data of the classical T Tauri star CI Tau collected with ESPaDOnS at the Canada-France-Hawaii Telescope, with the aims of detecting and characterizing the large-scale magnetic field that the star hosts, and of investigating how the star interacts with the inner regions of its accretion disc through this field. Our data unambiguously show that CI Tau has a rotation period of 9.0 d, and that it hosts a strong, mainly poloidal large-scale field. Accretion at the surface of the star concentrates within a bright high-latitude chromospheric region that spatially overlaps with a large dark photospheric spot, in which the radial magnetic field reaches  $-3.7$  kG. With a polar strength of  $-1.7$  kG, the dipole component of the large-scale field is able to evacuate the central regions of the disc up to about 50% of the co-rotation radius (at which the Keplerian orbital period equals the stellar rotation period) throughout our observations, during which the average accretion rate was found to be unusually high. We speculate that the magnetic field of CI Tau is strong enough to sustain most of the time a magnetospheric gap extending to at least 70% of the co-rotation radius, which would explain why the rotation period of CI Tau is as long as 9 d. Our results also imply that the 9-d radial velocity (RV) modulation that CI Tau exhibits is attributable to stellar activity, and thus that the existence of the candidate close-in massive planet CI Tau b to which these RV fluctuations were first attributed needs to be reassessed with new evidence.

**Key words:** stars: magnetic fields – stars: formation – stars: imaging – stars: individual: CI Tau – techniques: polarimetric

## 1 INTRODUCTION

Young protostars and pre-main-sequence (PMS) stars are ideal laboratories to assess theories of star / planet formation. This is especially true for investigating the key role that magnetic fields play in this process, e.g., when most of the initial angular momentum and magnetic flux inherited from the parent molecular cloud is removed from the central core (e.g., [Hennebelle & Teyssier 2008](#); [Vaytet et al. 2018](#)). At a later stage, the large-scale field of the star is found to be strong enough to evacuate the central regions of the accretion disc, forcing the star to co-rotate with the inner disc (e.g., [Bouvier et al. 2014](#); [Hartmann et al. 2016](#)), whereas disc fields are potentially able to affect how planets,

including massive giants, form and migrate within the disc (e.g., [Lin et al. 1996](#); [Muto et al. 2008](#)).

Both classical T Tauri stars (cTTs), still accreting from their surrounding accretion discs, and weak-line T Tauri stars (wTTs), no longer accreting from their depleted inner disc or having exhausted their disc entirely, are key targets for such studies. By unveiling their large-scale magnetic topologies using tomographic techniques such as Zeeman-Doppler Imaging (ZDI, [Semel 1989](#); [Brown et al. 1991](#); [Donati & Brown 1997](#); [Donati et al. 2006](#)) applied to phase-resolved spectropolarimetric data sets, one can quantitatively investigate how cTTs interact and exchange angular momentum with their discs (e.g., [Donati et al. 2011a](#)); by modelling their magnetic activity and in particular their surface brightness inhomogeneities, one can also reveal the potential presence of close-in giant planets or

★ E-mail: jean-francois.donati@irap.omp.eu

biting wTTSs (e.g., David et al. 2016; Donati et al. 2017b; Yu et al. 2017). Last but not least, one can study how dynamo processes operate within the convective interior / envelope of TTSs and generate their large-scale fields, to be compared with those of mature main-sequence low-mass stars (e.g., Morin et al. 2008; Donati & Landstreet 2009; Morin et al. 2010; Donati et al. 2011a; Gregory et al. 2012; Folsom et al. 2016).

Among the handful of cTTSs identified for observations within the MaPP and MaTYSSSE Large Programmes carried out at Canada-France-Hawaii Telescope (CFHT) with the ESPaDOnS spectropolarimeter, CI Tau, reported to potentially host a close-in giant planet (Johns-Krull et al. 2016; Biddle et al. 2018; Flagg et al. 2019), is thus especially interesting for tomographic studies based on spectropolarimetric monitoring. In this paper, we present ESPaDOnS observations of CI Tau collected from mid December 2016 to mid February 2017; following a short review of the evolutionary status of this cTTS, we analyze our new data in terms of the large-scale magnetic topologies that the newborn star hosts, and of the accretion patterns that the star-disc interactions trigger. We finally conclude our study with implications for our understanding of magnetospheric accretion in cTTSs, and for the candidate close-in giant planet CI Tau b.

## 2 EVOLUTIONARY STATUS OF CI TAU

To put our study on a firm footing and make it consistent with previous work, we start by revising the evolutionary status of CI Tau.

We apply to our best spectra of CI Tau (see Sec. 3) the spectral classification tool we developed and used previously (e.g., Donati et al. 2012); we derive a photospheric temperature of  $T_{\text{eff}} = 4200 \pm 50$  K and a logarithmic surface gravity of  $\log g = 3.6 \pm 0.2$  (in cgs units). We note that our temperature estimate is larger than the value often quoted in the literature (of 4060 K Kenyon & Hartmann 1995) but in good agreement with independent measurements from high-resolution spectroscopy (Schiavon et al. 1995), or more recent values from low-resolution spectrophotometry (Herczeg & Hillenbrand 2014). Given the published B – V color index of CI Tau (1.37, Grankin et al. 2007) and the one we expect for a young star of the same temperature ( $1.16 \pm 0.02$ , Pecaut & Mamajek 2013), we derive that the visual extinction the star suffers is  $A_V = 0.65 \pm 0.20$ <sup>1</sup>. The corresponding bolometric correction is equal to  $-0.89 \pm 0.02$  (Pecaut & Mamajek 2013).

From the minimum V magnitude (maximum brightness) of CI Tau ( $V = 12.28 \pm 0.10$ , Grankin et al. 2007) and assuming that CI Tau always features cool surface spots making it dimmer by at least  $0.25 \pm 0.10$  mag in V<sup>2</sup>, we derive a bolo-

metric magnitude of  $4.49 \pm 0.25$  using the accurate distance estimate from Gaia ( $158.7 \pm 1.2$  pc, Gaia Collaboration 2018). The corresponding logarithmic luminosity relative to the Sun ( $\log(L_\star/L_\odot) = 0.1 \pm 0.1$ ) translates into a mass and radius of CI Tau equal to  $M_\star = 0.9 \pm 0.1 M_\odot$  and  $R_\star = 2.0 \pm 0.3 R_\odot$  respectively when using the PMS evolutionary models of Siess et al. (2000, assuming solar metallicity and including convective overshooting); in this context, CI Tau is a  $2 \pm 1$  Myr star that has not yet started to develop an inner radiative core. Our mass estimate is in very good agreement with the dynamic value derived from radio interferometry (equal to  $0.90 \pm 0.02 M_\odot$ , Simon et al. 2017, 2019, which we use hereafter); our luminosity estimate is larger than the literature values (Andrews et al. 2013; Herczeg & Hillenbrand 2014), reflecting both the revised distance and our choice to compensate for the contribution of spots at the stellar surface.

The rotation period we derive for CI Tau ( $P_{\text{rot}} = 9.00 \pm 0.05$  d, see Sec. 3) and the line-of-sight-projected equatorial rotation velocity we measure ( $v \sin i = 9.5 \pm 0.5$  km s<sup>-1</sup>, see Sec. 5, with  $i$  noting the angle between the line of sight and the rotation axis of the star) imply that  $R_\star \sin i = 1.69 \pm 0.10 R_\odot$  and thus that  $i \approx 55^\circ$ , with potential values ranging from  $45^\circ$  up to  $90^\circ$ . This is consistent with the tilt of the disc rotation axis to the line of sight, reported to be in the range  $46^\circ$  to  $54^\circ$  (Guilloteau et al. 2014; Clarke et al. 2018). This agreement further supports our luminosity estimate and the associated radius value, and may even suggest that both are still slightly underestimated; given the reported values of  $v \sin i$  and  $P_{\text{rot}}$ , a lower luminosity and a smaller radius would indeed imply that the inclination of the star significantly differs from that of the disc. This places the co-rotation radius of CI Tau (i.e., the radius at which the Keplerian orbital period equals the stellar rotation) at a distance of  $r_{\text{cor}} = 0.082 \pm 0.001$  au or  $8.8 \pm 1.3 R_\star$  from the centre of the star, thereby setting the co-rotation velocity at  $99 \pm 1$  km s<sup>-1</sup> and its line-of-sight projection at  $76 \pm 5$  km s<sup>-1</sup> for a disc inclination of  $50 \pm 4^\circ$  (Guilloteau et al. 2014; Clarke et al. 2018), consistent with the RV semi-amplitude of the CO signature recently reported (equal to 77 km s<sup>-1</sup>, Flagg et al. 2019).

The fundamental parameters of CI Tau used in our study are summarized in Table 1.

## 3 SPECTROPOLARIMETRIC OBSERVATIONS

Our set of observations consists of 18 circularly polarized spectra collected over 2 months from mid December 2016 to mid February 2017 with the ESPaDOnS spectropolarimeter at CFHT, covering the domain 370–1,000 nm at a resolving power of 65,000 (Donati 2003). Raw frames were reduced with the standard ESPaDOnS reduction package (Libre ESPrIT), and Least-Squares Deconvolution (LSD, Donati et al. 1997) was applied to all reduced spectra, using a line list appropriate to CI Tau. The full journal of observations is presented in Table 2. The first Stokes  $I$  spectrum

<sup>1</sup> In doing so, we assume that veiling (see Sec. 3) and cool surface spots (see Sec. 5), having opposite effects on photometric colors, more or less cancel out within the quoted error bar on  $A_V$ .

<sup>2</sup> Here we refer not only to large-scale spots like those reconstructed in Sec. 5, but also to small-scale ones evenly distributed over the star and generating little to no rotational modulation as in, e.g., Gully-Santiago et al. (2017). The chosen value of  $0.25 \pm 0.10$  corresponds to the residual magnitude increase that is not compensated by minimum veiling at maximum brightness

(see Sec. 5), implying that the dimming from dark spots only is in fact larger. The average V magnitude of CI Tau (Grankin et al. 2007,  $V = 13.11 \pm 0.10$ ,) indicates that about two thirds of the stellar surface are usually covered with spots.

**Table 1.** Summary of the fundamental parameters of CI Tau used in our study (all estimates are from our work except where noted)

$T_{\text{eff}}$ (K)	$4200 \pm 50$	
$\log(L_{\star}/L_{\odot})$	$0.1 \pm 0.1$	
$M_{\star}$ ( $M_{\odot}$ )	$0.9 \pm 0.1$	Siess et al. (2000)
	$0.90 \pm 0.02$	Simon et al. (2019)
$R_{\star}$ ( $R_{\odot}$ )	$2.0 \pm 0.3$	Siess et al. (2000)
age (Myr)	$2.0 \pm 1.0$	Siess et al. (2000)
distance (pc)	$158.7 \pm 1.2$	Gaia Collaboration (2018)
$P_{\text{rot}}$ (d)	$9.00 \pm 0.05$	
$i$ ( $^{\circ}$ )	$55^{+35}_{-10}$	
$i_{\text{disc}}$ ( $^{\circ}$ )	$50 \pm 4$	Guilloteau et al. (2014)
$v \sin i$ ( $\text{km s}^{-1}$ )	$9.5 \pm 0.5$	
$v_{\text{rad}}$ ( $\text{km s}^{-1}$ )	$16.8 \pm 0.2$	
$v_{\text{esc}}$ ( $\text{km s}^{-1}$ )	$415 \pm 30$	
$r_{\text{cor}}$ (au)	$0.082 \pm 0.001$	$8.8 \pm 1.3 R_{\star}$
$\log \dot{M}$ ( $M_{\odot} \text{ yr}^{-1}$ )	$-7.6 \pm 0.3$	from H $\alpha$ , H $\beta$ and He I $D_3$

of CI Tau we collected (at cycle 0.011) was slightly affected by moonlight whose spectrum shows up in the far blue wing of the corresponding LSD profile. This pollution, occurring far enough in the profile wings not to affect our analysis, was nonetheless filtered with the technique devised in this purpose (Donati et al. 2017b).

Radial velocities (RVs) of the Stokes  $I$  LSD photospheric profiles of CI Tau (computed from the first moment of the unpolarized profiles, see Fig. 1 top left panel) are clearly modulated with a period of  $9.02 \pm 0.06$  d; although the RV variations are largely sinusoidal, adding the first harmonics significantly improves the fit, with the corresponding reduced chi-square ( $\chi_r^2$ ) showing a single deep and narrow minimum within a wide range of periods (5 to 16 d) and featuring a false alarm probability of order 0.1%. We also note that LSD profiles are exhibiting strong asymmetries at times, with bisector spans (BSs) varying with time (see Fig. 2) and being modulated with a period of  $8.9 \pm 0.1$  d.

Zeeman signatures from large-scale surface magnetic fields are detected (with a false alarm probability smaller than 0.1%, and in most cases smaller than 0.001%) in all circular polarisation (Stokes  $V$ ) LSD profiles of CI Tau. The corresponding longitudinal fields (i.e., line-of-sight projected magnetic fields averaged over the visible hemisphere) probed by Stokes  $V$  LSD profiles range from  $-25$  to  $95$  G (see Fig. 1 bottom left panel), and are found to vary with a period  $9.04 \pm 0.08$  d, i.e., very close to that of the RVs variations of Stokes  $I$  LSD profiles; adding the first harmonics to the sinusoidal fit is essential given the two unequal minima and maxima that the measured longitudinal fields exhibit over one period.

#### 4 VEILING AND ACCRETION

The amount of veiling<sup>3</sup> that the LSD profiles are subject to (compared to those of a wTTS of similar spectral type) is found to vary between 0.5 and 2.5 (see Fig. 1 middle left panel). These fluctuations feature a significant amount of intrinsic variability, as is often the case with veiling and more generally with accretion-related phenomena; they also include a modulated component exhibiting a period of  $8.7 \pm 0.2$  d, slightly smaller though still compatible with that inferred from the modulation of RVs and longitudinal fields. By computing LSD signatures for blue and red spectral regions separately (with weighted-average central wavelengths of 520 and 740 nm respectively), we find that both the average veiling and its modulation are 2.3 $\times$  stronger in the blue than in the red, consistent with what is expected for veiling in cTTSs. We also note that the veiling in our optical spectra of CI Tau is typically 3 $\times$  larger than that reported in previous studies (e.g., Hartigan et al. 1995; Beristain et al. 2001; Herczeg & Hillenbrand 2014), suggesting that the star is either more actively accreting and / or that its photosphere is intrinsically fainter (with respect to the main veiling sources).

Accretion at the surface of the star is best probed with the He I  $D_3$  line complex at 587.56 nm (see Fig. 3 left panel), exhibiting in particular less intrinsic variability than veiling and offering at the same time the additional capability of estimating magnetic fields within accretion regions (Johns-Krull et al. 1999). In cTTSs actively accreting from their inner discs like CI Tau, this He I feature usually exhibits both a narrow core emission component (NC) probing the post-shock region close to the stellar surface and located at the footpoint of the magnetized funnels, and a broad emission component (BC) coming either from the accretion funnels linking the star to the inner disc and / or from a hot wind likely powered by interactions between the magnetosphere and the inner disc (Beristain et al. 2001). In agreement with this picture, we find that Stokes  $V$  Zeeman signatures in the He I  $D_3$  line of CI Tau are only detected in conjunction with the NC, i.e., where the magnetic field is expected to be strongest and the velocity gradient of the emitting plasma to be smallest. The BC of CI Tau is typically 5 $\times$  broader and stronger than the NC, which features an average (veiled) equivalent width (EW) and full-width-at-half-maximum of 20 and 40  $\text{km s}^{-1}$  (0.04 and 0.08 nm) respectively when most intense.

Both EWs and RVs of the He I  $D_3$  NC are clearly modulated with time in CI Tau (see Fig. 1 middle and top central panels), with respective periods of  $9.1 \pm 0.2$  and  $9.0 \pm 0.2$  d. EWs and RVs of the BC (not shown) are also variable with time, but anti-correlated with the NC; when corrected for the veiling, the BC no longer shows consistent periodic fluc-

<sup>3</sup> Veiling is a consequence of accretion, in particular shocks occurring at the surface of the star and potential interactions between the magnetosphere and the inner accretion disc (e.g., Beristain et al. 2001), that generate a mostly featureless continuum, stronger in the blue than in the red, that adds up on the stellar spectrum and reduces the depths, or 'veils', the line profiles. The values we show here (see Fig. 1) represent the excess continuum flux relative to that from the stellar photosphere, at an average wavelength of about 620 nm.

**Table 2.** Journal of ESPaDOnS observations of CI Tau from December 2016 to February 2017. All observations consist of sequences of 4 subexposures, each lasting either 1200 s (first 8 spectra) or 1000 s (last 10 spectra). Columns respectively list, for each observation, the UT date, time, Barycentric Julian Date (BJD), peak signal to noise ratio S/N (per  $2.6 \text{ km s}^{-1}$  velocity bin), rms noise level in Stokes  $V$  LSD profiles, rotation cycle  $c$  computed using ephemeris BJD ( $d = 2457736.7 + 9.0c$ ), longitudinal fields  $B_\ell$  measured from both LSD profiles and He I  $D_3$  narrow emission component (NC), the RVs and bisector spans (BSs) of LSD profiles, and the RVs of the He I  $D_3$  NC.

Date	UT (hh:mm:ss)	BJD (2,457,736+)	S/N	$\sigma_{\text{LSD}}$ (0.01%)	$c$	$B_{\ell\text{LSD}}$ (G)	$B_{\ell\text{He}}$ (kG)	RV <sub>LSD</sub> ( $\text{km s}^{-1}$ )	BS <sub>LSD</sub> ( $\text{km s}^{-1}$ )	RV <sub>He</sub> ( $\text{km s}^{-1}$ )
2016 Dec 14	07:01:06	0.79801	160	3.0	0.011	$95 \pm 11$	$-1.15 \pm 0.49$	$16.7 \pm 0.3$	$0.0 \pm 0.3$	$22.1 \pm 0.3$
2016 Dec 15	07:08:38	1.80322	160	3.0	0.123	$70 \pm 10$	$-1.70 \pm 0.48$	$17.4 \pm 0.3$	$-0.3 \pm 0.3$	$21.4 \pm 0.3$
2016 Dec 21	08:12:55	7.84769	170	3.0	0.794	$48 \pm 11$	$-1.31 \pm 0.50$	$16.8 \pm 0.3$	$-0.3 \pm 0.3$	$27.6 \pm 0.3$
2016 Dec 22	08:30:34	8.85991	180	2.6	0.907	$15 \pm 11$	$-2.46 \pm 0.74$	$17.3 \pm 0.3$	$-0.7 \pm 0.3$	$24.4 \pm 0.3$
2017 Jan 08	08:53:59	25.87534	180	2.7	2.797	$-21 \pm 10$	$-0.55 \pm 0.66$	$17.4 \pm 0.3$	$-0.5 \pm 0.3$	$23.2 \pm 0.3$
2017 Jan 09	09:50:38	26.91461	180	2.6	2.913	$-3 \pm 10$	$-0.98 \pm 0.61$	$16.9 \pm 0.3$	$-0.0 \pm 0.3$	$23.6 \pm 0.3$
2017 Jan 11	06:10:15	28.76144	150	3.3	3.118	$95 \pm 12$	$-3.49 \pm 0.52$	$17.7 \pm 0.3$	$-0.3 \pm 0.3$	$22.8 \pm 0.3$
2017 Jan 13	11:37:52	30.98881	160	3.0	3.365	$-25 \pm 13$	$-1.27 \pm 0.38$	$17.7 \pm 0.3$	$-0.7 \pm 0.3$	$22.8 \pm 0.3$
2017 Jan 15	10:47:14	32.95351	140	3.6	3.584	$60 \pm 16$	$0.05 \pm 0.46$	$14.8 \pm 0.3$	$1.2 \pm 0.3$	$27.6 \pm 0.3$
2017 Jan 16	09:53:01	33.91579	140	3.5	3.691	$21 \pm 19$	$0.17 \pm 0.85$	$15.2 \pm 0.3$	$0.2 \pm 0.3$	$22.7 \pm 0.3$
2017 Jan 21	07:27:14	38.81418	160	3.0	4.235	$19 \pm 14$	$-2.08 \pm 0.30$	$18.8 \pm 0.3$	$-0.4 \pm 0.3$	$22.2 \pm 0.3$
2017 Jan 23	07:30:47	40.81649	160	3.1	4.457	$33 \pm 17$	$-0.72 \pm 0.34$	$15.0 \pm 0.3$	$2.1 \pm 0.3$	$27.4 \pm 0.3$
2017 Feb 04	06:42:27	52.78190	170	3.0	5.787	$7 \pm 12$	$-0.55 \pm 0.51$	$16.4 \pm 0.3$	$-0.1 \pm 0.3$	$24.6 \pm 0.3$
2017 Feb 05	06:26:56	53.77103	150	3.3	5.897	$-19 \pm 12$	$-1.91 \pm 0.70$	$16.8 \pm 0.3$	$0.2 \pm 0.3$	$23.7 \pm 0.3$
2017 Feb 14	07:33:52	62.81665	160	3.1	6.902	$16 \pm 12$	$-2.42 \pm 0.69$	$16.5 \pm 0.3$	$0.5 \pm 0.3$	$23.8 \pm 0.3$
2017 Feb 15	07:22:41	63.80880	160	3.0	7.012	$85 \pm 13$	$-2.38 \pm 0.66$	$16.3 \pm 0.3$	$0.6 \pm 0.3$	$22.2 \pm 0.3$
2017 Feb 16	07:27:28	64.81202	150	3.3	7.124	$93 \pm 14$	$-1.51 \pm 0.59$	$17.7 \pm 0.3$	$-0.1 \pm 0.3$	$23.1 \pm 0.3$
2017 Feb 17	07:37:19	65.81876	180	2.7	7.235	$22 \pm 18$	$-1.84 \pm 0.49$	$19.0 \pm 0.3$	$-0.3 \pm 0.3$	$19.8 \pm 0.3$

tuations of its EW but rather intrinsic variability about an average strength of about  $240 \text{ km s}^{-1}$  (0.47 nm), whereas the NC exhibits an even stronger modulation of its EW, now peaking at about  $70 \text{ km s}^{-1}$  (0.14 nm). Zeeman signatures are detected at most epochs in the Stokes  $V$  profile of the He I  $D_3$  NC of CI Tau, probing magnetic fluxes at the bottom of accretion funnels. The corresponding longitudinal fields are found to range from 0 to  $-2.5 \text{ kG}$  (and even  $-3.5 \text{ kG}$  in a single case, see Fig. 1 bottom central panel) with a median error bar of  $0.5 \text{ kG}$ , and to be modulated with a period of  $8.9 \pm 0.2 \text{ d}$ , in good agreement with all other periods identified so far in our data set.

The Ca II infrared triplet (IRT) was also shown to probe accretion regions of cTTSs (e.g., Muzerolle et al. 1998), albeit more ambiguously than the He I  $D_3$  line as a result of the chromospheric activity often contributing significantly to the NC (Donati et al. 2011a). In the case of CI Tau, the Ca II IRT also features both a NC and a BC, with the BC being typically  $10\times$  broader and  $40\times$  stronger than the NC. Given the strong intensity contrast between both components and the often complex shape of the BC, reliably extracting (with a multiple Gaussian fit) the much weaker NC is tricky. Whereas the NC exhibits RVs that vary with a period of  $9.1 \pm 0.6 \text{ d}$ , its EW, equal to  $18 \text{ km s}^{-1}$  or  $0.05 \text{ nm}$  in average (in the veiled spectrum), is not seen to fluctuate in a clear periodic way (see Fig. 1 top and middle right panels), presumably as the result of a high level of intrinsic variability in the dominant contribution from chromospheric activity. Zeeman signatures in the Stokes  $V$  LSD profiles of the Ca II IRT NC are detected most of the times, with longitudinal fields in the range  $-60$  to  $-740 \text{ G}$  with a median error bar of  $70 \text{ G}$  (see Fig. 1 bottom right panel). These longitudinal fields are typically  $5\times$  weaker than those inferred

from the He I NC, indicating that accretion contributes to about 20% of this emission whereas chromospheric activity contributes to 80% (assuming that magnetic fields in accretion regions are much stronger than those in non-accreting ones, as expected from previous studies). As for EWs, longitudinal fields of the Ca II IRT NC exhibit a high level of intrinsic variability and show no more than a hint of periodicity (with a period of  $8.0 \pm 0.3 \text{ d}$ ).

Given that most spectral features of CI Tau, and in particular photospheric LSD profiles and the He I  $D_3$  NC reliably probing accretion post-shock regions near the surface of the star, are observed to fluctuate in a regular way over our 2-month observing run with a clear period of  $9.0 \text{ d}^4$ , we conclude that this period is almost certainly the rotation period of the star. Moreover, the reported variability of CI Tau is found to be very similar to that of other cTTSs (Donati et al. 2011a,b, 2012), coming as further evidence that what we see is truly rotational modulation. It logically follows that the main 9 d period detected in the photometric light curve of CI Tau collected with the K2 space probe during campaign 13 on Taurus between 2017 March 07 and May 27 (Biddle et al. 2018), i.e., about 1–3 months after the end of our ESPaDOnS run, is attributable to rotational modulation caused by brightness features at the surface of the star carried in and out of the observer’s view. We stress that the 9-d period is not only the dominant one, but also the only one that shows up consistently in all our time series; by contrast, the period of  $6.6 \text{ d}$  also present in the K2 data (as the third strongest peak in the periodogram in the period range 5–16 d) and previously suggested to be the

<sup>4</sup> The weighted average of all periods measured from both LSD profiles and the He I  $D_3$  NC is  $9.00 \pm 0.05 \text{ d}$ .



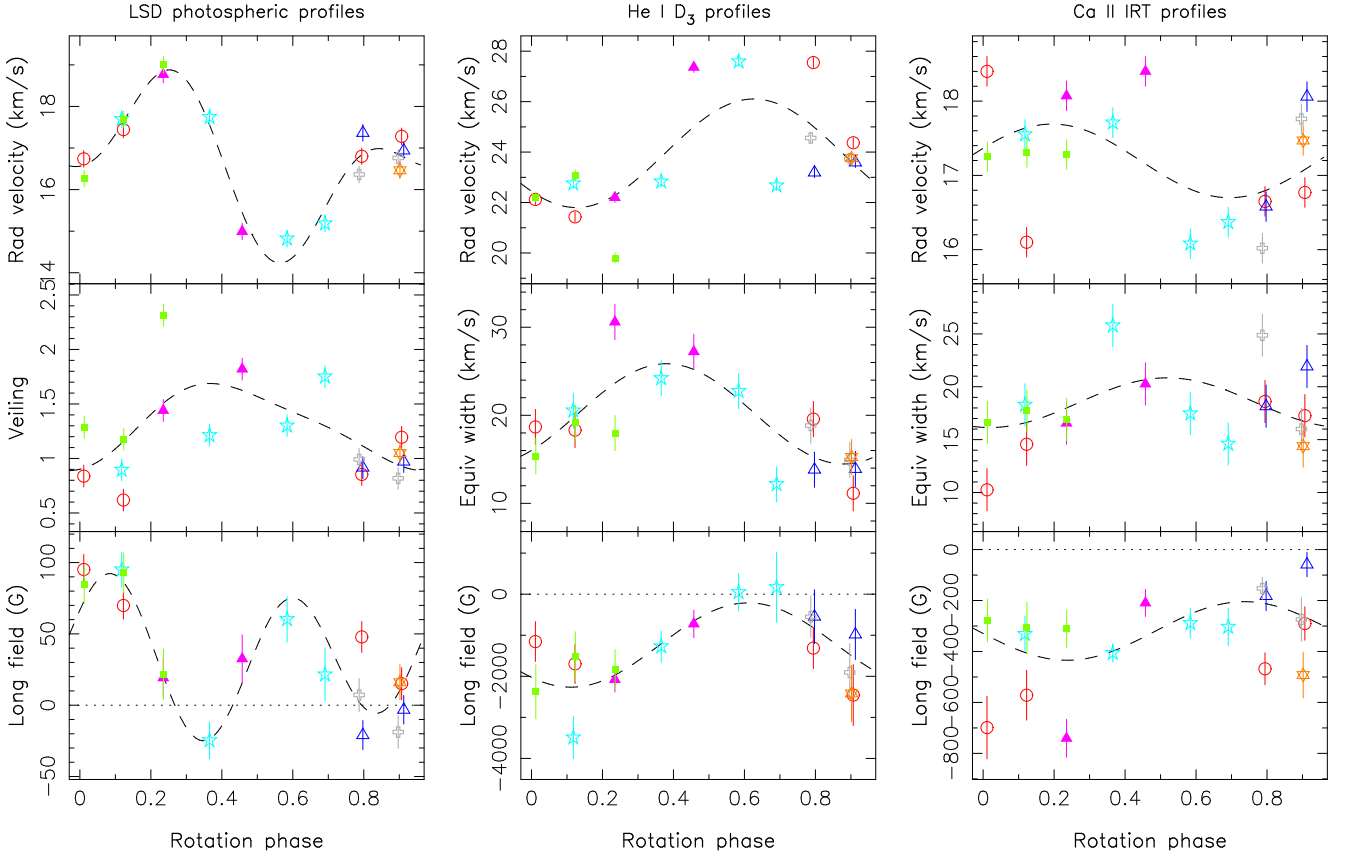


**Figure 1.** Variability and modulation of the LSD profiles (left panel), He I  $D_3$  (middle panel) and Ca II IRT (right panel) NCs of CI Tau as a function of rotation phase (computed with the ephemeris of Table 2 assuming a rotation period of 9.0 d). Each panel shows the RVs (top), the veiled EWs (or veiling in the case of LSD profiles, middle) and the longitudinal fields (bottom). The red open circles, blue open triangles, cyan open pentagrams, purple filled triangles, open grey pluses, orange open hexagrams and filled green squares respectively depict measurements obtained during rotation cycles 0, 2, 3, 4, 5, 6 and 7. The dashed lines show sine (plus first harmonic in the case of LSD profiles) fits to the data to emphasize modulation. Positive longitudinal fields correspond to fields pointing towards the observer.

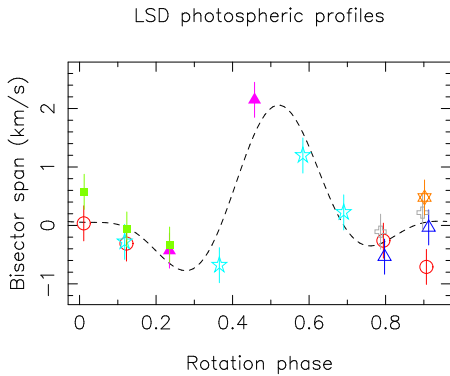


**Figure 2.** Same as Fig. 1 for the LSD-profile BSs of CI Tau. The sine fit to the data now includes the first two harmonics to better track the rapid temporal variability of BSs (e.g., Hébrard et al. 2014)

rotation period of CI Tau (Biddle et al. 2018), is not seen in the (veiled or unveiled) EW of the He I NC (whose 9-d modulation is quite clear, see Fig. 1 middle central panel), and only marginally (in the range 6.8–7.0 d, along with several other weak peaks of comparable strengths) in the RVs and longitudinal fields of the He I line and LSD photospheric

lines. We thus phased our data using a rotational period of 9.0 d (see ephemeris in Table 2).

In this context, our data (see Fig. 1) suggest that the main accretion region is located at phase 0.3–0.4, i.e., when both the He I NC and the veiling are strongest. Bisector variations in LSD profiles further confirm that the 9-d modulation is caused by the presence of surface features, known to distort spectral features, rather than by, e.g., an orbiting body that would shift the spectral lines without affecting their shapes and bisectors. RV curves of LSD profiles and of He I NC further indicate that the accretion region is dark at photospheric level and bright at chromospheric level, and that the post-shock zone in which the He I NC forms is in average red-shifted with respect to the stellar rest-frame by about  $7 \text{ km s}^{-1}$ . The main accretion region apparently coincides with strong magnetic fields of up to  $\approx 3 \text{ kG}$ , causing it to appear dark at photospheric level with respect to the less-magnetic, non-accreting surroundings, and thereby making the strong fields to go undetected in LSD profiles. We also report that the K2 brightness of CI Tau is minimum (by about 15%) when veiling is maximum, indicating that the observed brightness modulation mostly relates to the surface distribution of photospheric features and in particular to the presence of the dark accretion region mentioned above; it even suggests that veiling variations are in fact dominated

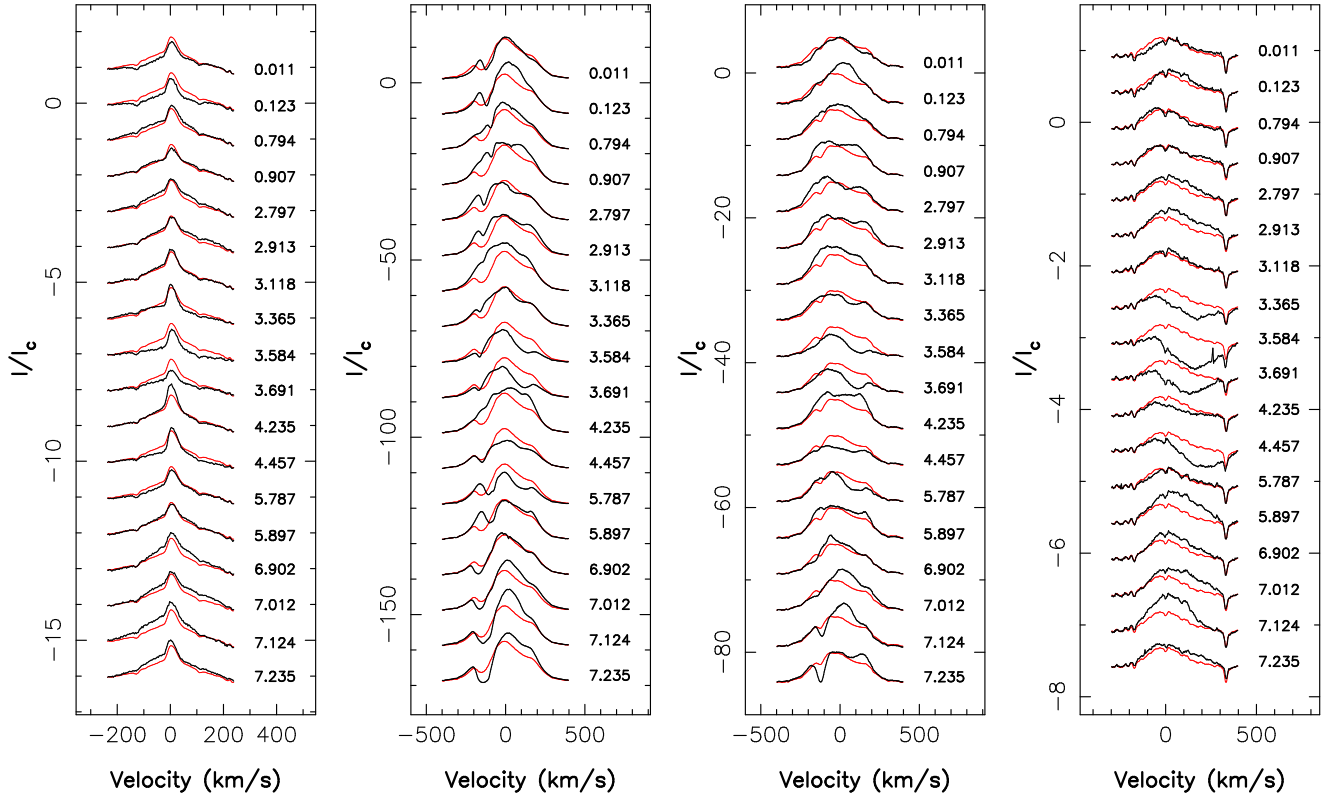


**Figure 3.** From left to right, He I  $D_3$ ,  $H\alpha$ ,  $H\beta$  and 777.19 nm O I profiles of CI Tau throughout our observing run. The red line depicts the average profile over the run to emphasize temporal variations. Note the different scales on both x and y axes.

by the periodic changes in the photospheric brightness of CI Tau rather than by fluctuations in the veiling sources themselves, consistent with the fact that the intensity of the He I BC (associated with the main veiling source) exhibits no obvious rotational modulation. More quantitative results require a full tomographic analysis, which we carry out in the following section.

From the unveiled peak EW of the He I NC that we observe for CI Tau (about  $70 \text{ km s}^{-1}$  or  $0.14 \text{ nm}$  once averaged over the successive cycles), we can compute the peak logarithmic flux in the line ( $-4.5$  in units of  $L_\odot$ ), translate it into a peak logarithmic accretion luminosity ( $-1.1$  in units of  $L_\odot$ , using empirical calibrations of Fang et al. 2009), and estimate a logarithmic mass accretion rate of  $-8.2 \pm 0.3$  (in units of  $M_\odot \text{ yr}^{-1}$ ). Repeating the same calculation for the (unmodulated) He I BC, we derive logarithmic line flux, accretion luminosity and accretion rate of  $-3.9$ ,  $-0.4$  and  $-7.4$  respectively (in the same units as for the NC). At this point, it is unclear whether the mass accretion rates derived independently from the He I NC and BC have any physical interpretation, or whether they only make sense when considered together; we come back on this point in Sec. 6. The contrast between the accretion luminosities of the He I BC and NC (about  $0.7$  in log) is consistent with the ratios of featureless continua associated with both components, which can be estimated from the observed modulation amplitudes of the veiling and of the K2 photometric flux, and from the assumption that only the continuum associated with the NC happens to be modulated with rotation (in phase with the EW of the NC).

Balmer lines of CI Tau (see Fig. 3 middle panels), also

in emission, feature average (unveiled) equivalent widths of  $8500$  and  $3800 \text{ km s}^{-1}$  respectively ( $18.6$  and  $6.2 \text{ nm}$ ), translating into logarithmic line fluxes, accretion luminosities and mass accretion rates of  $-2.3$ ,  $-0.6$  and  $-7.7$  for  $H\alpha$  and  $-2.9$ ,  $-0.7$  and  $-7.8$  for  $H\beta$  (in units of  $L_\odot$ ,  $L_\odot$  and  $M_\odot \text{ yr}^{-1}$ ).

Both lines also feature conspicuous red-shifted absorption components (with respect to the mean profile) at cycles  $3.584$ ,  $3.691$ ,  $4.457$  and  $5.787$ , likely tracing accretion funnels transiting the stellar disc as the star rotates, suggesting that accretion occurs towards polar (rather than equatorial) regions given the inclination of the rotation axis (see Sec. 2). Even stronger red-shifted absorption is observed in the  $777.19 \text{ nm}$  O I line (see Fig. 3 right panel) with the red wing extending up to a velocity of  $380 \text{ km s}^{-1}$  with respect to the star at cycles  $3.584$  and  $4.457$ , corresponding to  $92 \pm 7\%$  of the escape velocity of CI Tau (equal to  $v_{\text{esc}} = 415 \pm 30 \text{ km s}^{-1}$ , see Table 1).

Finally we report time-variable blue-shifted narrow absorption features in both  $H\alpha$  and  $H\beta$  at velocities in excess of  $100 \text{ km s}^{-1}$  (see Fig. 3 middle panels, at cycles  $7.124$  and  $7.235$ , but also present in  $H\alpha$  only at many other phases), suggesting that intermittent magnetospheric ejection phenomena are taking place in the circumstellar environment of CI Tau. We come back on these points in Sec. 6.

## 5 TOMOGRAPHIC MODELLING OF CI TAU

To recover the large-scale magnetic field at the surface of CI Tau simultaneously with maps of the photospheric brightness and of the accretion-induced emission in the He I  $D_3$  line

at chromospheric level, we use the tomographic approach called Zeeman-Doppler Imaging. This is achieved as in previous similar papers (e.g., Donati et al. 2019), with one significant difference. In the present study, we used the He I  $D_3$  NC as the accretion proxy, rather than the Ca II IRT profiles that were found to be poorly informative about accretion regions at the surface of CI Tau (see Sec. 4). The main disadvantage of the He I  $D_3$  NC is that they usually exhibit asymmetric local Stokes  $I$  profiles, and local Stokes  $V$  profiles departing significantly from antisymmetry (i.e., with stronger / narrower blue lobes and shallower / broader red lobes on both sides of the line center, see, e.g., the top panel of Fig. 3 in Donati et al. 2011a, as a result of the velocity gradients in the line formation region), rendering them less straightforward to model than the more standard Ca II IRT profiles. In the case of CI Tau however, the intrinsic variability of the Ca II IRT NC gives us no other choice than to apply our model to the He I  $D_3$  profiles.

The main steps of the imaging process are as follows. Starting from featureless images, ZDI iteratively adds information on the stellar surface maps to optimise the fit to the observations using conjugate gradient techniques, until data are fitted at a given  $\chi^2_r$  level. Maps of the photospheric brightness (assuming cool spots only) and of the accretion-induced He I NC (assuming bright chromospheric accretion regions only) are described as grids of independent pixels, whereas the poloidal and toroidal components of the large-scale fields are expressed as series of spherical harmonics (SH, Donati et al. 2006), truncated to modes with  $\ell \leq 7$  in the case of CI Tau. We further assume that the field is mostly antisymmetric with respect to the centre of the star (i.e., that odd SH modes dominate, as in, e.g., Donati et al. 2011a), so that accretion funnels linking the inner disc to the star are anchored at high latitudes, as often reported for cTTSs (e.g., from the amplitude of the RV modulation of accretion lines, see Fig. 1 top central panel).

To approximate the local Stokes  $I$  and  $V$  profiles of both photospheric absorption and He I NC profiles at each point of the stellar surface, we use Unno-Rachkovsky’s analytical solution to the polarized radiative transfer equations in a Milne-Eddington atmosphere, taking into account the local values of the various relevant parameters, i.e., radial velocity and limb darkening (for all maps), relative photospheric brightness (for the photospheric brightness and magnetic maps), accretion-induced He I emission at chromospheric level (for the He I emission and magnetic maps) and magnetic field (for all maps). We then integrate local profiles over the whole visible hemisphere to infer the synthetic profiles of CI Tau at each observed epoch. A magnetic filling factor of 30% over the whole stellar surface was assumed for our study, applying both to LSD profiles and He I NC as in our previous papers (e.g., Donati et al. 2010). Velocity gradients within the He I line formation region are not taken into account, implying that our model is not capable of reproducing asymmetries of the local He I Stokes  $I$  and  $V$  profiles.

The fit to our data that ZDI obtains is shown in Fig. 4 for both the LSD photospheric and He I NC profiles (left and right panels respectively). Overall, we find that Stokes  $I$  and  $V$  profiles and their first order moments (i.e., the RVs and longitudinal fields) are well reproduced, especially given the large amount of intrinsic variability that the spectra of

CI Tau exhibits. As expected from the limitations of our model, the fit to the Stokes  $V$  profiles of the He I core emission is less accurate (see below for a more detailed description). We find that the  $v \sin i$  providing the best match to the far wings of the Stokes  $I$  profiles is  $9.5 \pm 0.5 \text{ km s}^{-1}$ , whereas the optimal average RV of CI Tau is  $v_{\text{rad}} = 16.8 \pm 0.2 \text{ km s}^{-1}$  (consistent with most young stars in the Taurus cloud, Galli et al. 2018).

One can note from Fig. 4 (left panel) that the RV variations of LSD profiles (reaching a peak-to-peak amplitude of  $4 \text{ km s}^{-1}$ , see Fig. 1) and the corresponding BS changes (see Fig. 2) are attributable to profile distortions and asymmetries (e.g., at cycles 3.584 and 4.457) rather than to global line shifts (caused by, e.g., an orbiting body) that would generate neither profile asymmetries nor bisector changes; this demonstrates that the RV curve of CI Tau reflects mostly stellar activity and more specifically the presence of surface features. We also note that the amplitude of the RV modulation is found to be slightly larger in the blue than in the red (by about 10% between 520 and 740 nm), as expected from activity (e.g., Reinert et al. 2010).

This conclusion is further confirmed by ZDI, demonstrating that CI Tau hosts a high-latitude dark spot at phase 0.35–0.40, large enough (about 20% of the overall stellar surface, see Fig. 5, bottom left panel) to generate the observed variability of LSD profiles and the corresponding RV fluctuations (with the change from maximum to minimum RV occurring from phase 0.25 to 0.55, see Fig. 1). Although the main reconstructed dark spot itself is quite reliable, its detailed shape and the surrounding low-latitude features and appendages are subject to caution as they may reflect tomographic imaging spuriously translating stochastic profile variability (caused by accretion) into small surface structures with limited visibility, when phase coverage is moderate.

The surface map of He I emission in the NC clearly shows a well-defined accretion region located at phase 0.35 and latitude  $60^\circ$ , and covering  $\approx 3\%$  of the overall stellar surface (see Fig. 5, bottom right panel). This is again consistent with the phase at which emission in the He I NC peaks, as well as with the observed RVs of the He I NC (changing from minimum to maximum RV between phase 0.1 and 0.6, see Fig. 1). ZDI performs a fair job at reproducing the changes in the NC profile (see Fig. 4 third panel), although not the sharp blue side and smooth red side at maximum emission (e.g., at cycle 3.365) that reflect the intrinsic asymmetry of the local He I NC which our model does not incorporate.

The large-scale magnetic field that ZDI reconstructs is mostly poloidal, with a toroidal component that encompasses only  $\approx 15\%$  of the reconstructed magnetic energy (see Fig. 5, top panels). Its main feature is a large (negative) radial field region at phase 0.35 and latitude  $60^\circ$ , where the field flux reaches values down to  $-3.7 \text{ kG}$ , in agreement with peak longitudinal fields derived from He I emission profiles; this feature roughly overlaps with the extended dark spot at photospheric level and the main accretion region at chromospheric level that our Stokes  $I$  LSD and He I profiles revealed, confirming that accretion at the surface of CI Tau takes place at its high-latitude magnetic poles. The reconstructed toroidal field component causes magnetic field lines in the main radial field region to be more tilted towards the

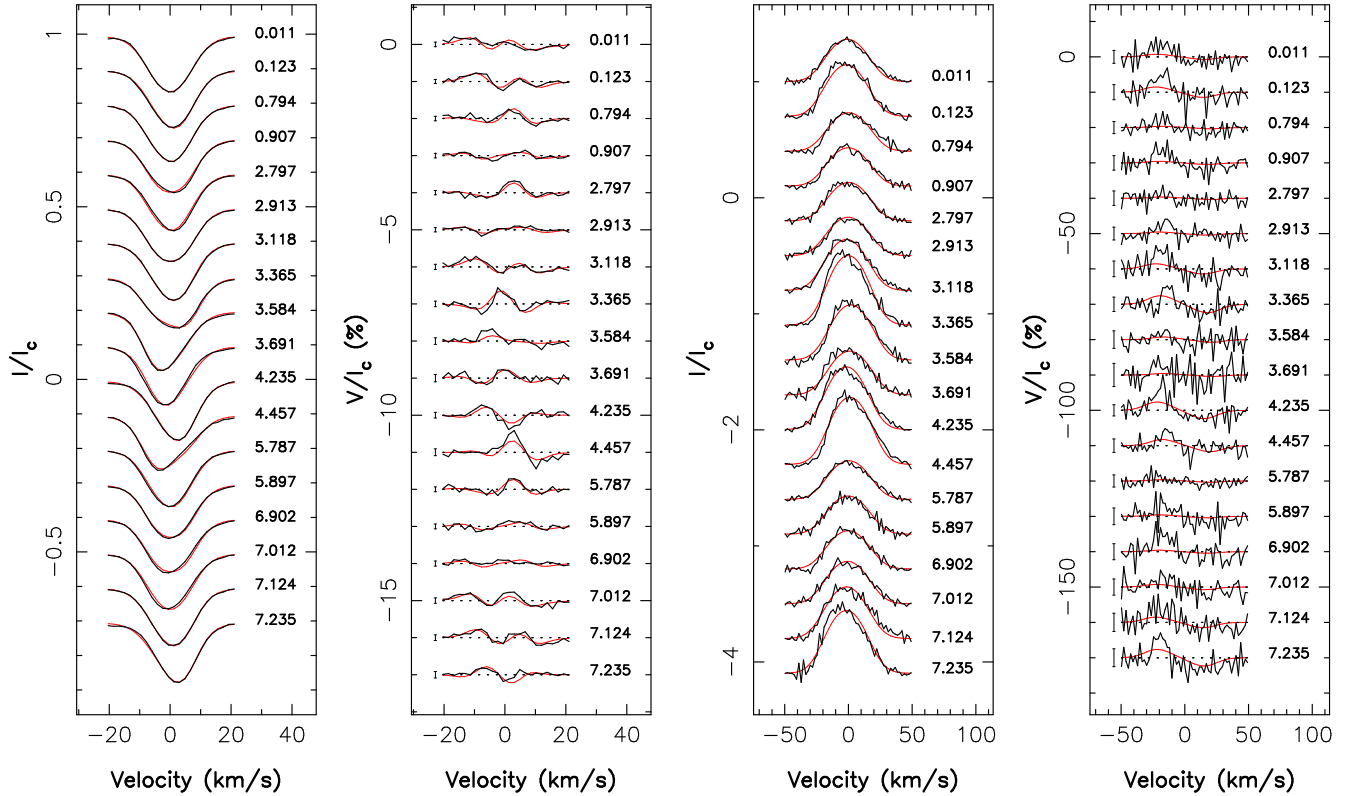


**Figure 4.** Observed (thick black line) and modelled (thin red line) LSD Stokes  $I$  and  $V$  profiles of the photospheric lines (left panels) and of the He I  $D_3$  core-emission profiles (right panels) of CI Tau. Rotation cycles and  $\pm 1\sigma$  error bars (for Stokes  $V$  profiles only) are indicated to the right and left of each observation respectively.

equatorial plane than those of the poloidal component; this is likely a real feature and a direct consequence of on-going accretion from the disc.

We note that the shapes of LSD Stokes  $V$  profiles are well fitted by our model (see Fig. 4 second panel), with small departures from the data (e.g., at cycle 4.457) presumably attributable to intrinsic variability. The shapes of Stokes  $V$  He I NC profiles, and in particular the stronger / narrower blue lobes and the shallower / broader red lobes of the detected Zeeman signatures, are less well reproduced, with only their average intensities being matched by ZDI; this again reflects the limitation of our model at describing local Stokes  $V$  profiles at the surface of the star that are not antisymmetric with respect to the local line center. This limitation is however not critical as our simple model is still able to grasp the fields needed to reproduce the average sizes of the blue and red lobes of the detected Zeeman signatures.

The inferred large-scale field of CI Tau mainly consists of a  $-1.7$  kG dipole component (tilted at  $20^\circ$  with respect to the rotation axis towards phase 0.5 and enclosing about 60% of the reconstructed magnetic energy) and of an octupole component of similar strength, with both being more or less aligned and parallel to each other. Depending on how the respective weights of Stokes  $I$  and  $V$  profiles are balanced in the imaging process, we infer dipole strengths varying by about 15%, i.e., from 1.5 to 2.0 kG (corresponding to 40–80% of the reconstructed magnetic energy).

We stress that modelling both LSD and He I emission profiles simultaneously is essential to reliably unveil the main properties of the large-scale field of CI Tau. For instance, the

dipole fields ZDI infers when applied to He I or LSD profiles only are respectively equal to 3.9 kG and 0.3 kG, i.e., over- or under-estimated by typical factors ranging from  $2.3\times$  to  $6\times$  with respect to the value inferred from modeling both sets consistently; whereas Zeeman signatures of the He I NC are critical to constrain field strengths within accretion regions (as demonstrated in Donati et al. 2007), simultaneously adjusting photospheric LSD profiles ensures that the relative areas of accreting and non-accreting regions, that depends on the relative intensities of the dipole and octupole components, are consistent with observations.

## 6 SUMMARY AND DISCUSSION

Using ESPaDOnS at CFHT, we carried out a spectropolarimetric monitoring of the cTTS CI Tau from mid December 2016 to mid February 2017. From a detailed analysis of its spectral lines, we find that CI Tau is a  $\approx 2$  Myr star with a mass of  $0.9 \pm 0.1 M_\odot$  and a radius of  $2.0 \pm 0.3 R_\odot$  according to the evolution models of Siess et al. (2000); the mass we derive agrees well with the most recent dynamic estimate from radio interferometry ( $0.90 \pm 0.02 M_\odot$ , Simon et al. 2019). Clear Zeeman signatures are detected in both photospheric and accretion lines of CI Tau, demonstrating that the star hosts a strong large-scale magnetic field.

Stokes  $I$  and  $V$  LSD profiles of photospheric lines and of the He I  $D_3$  accretion-induced NCs are found to be modulated with a clear period of  $9.00 \pm 0.05$  d, with temporal variations (e.g., in RVs and BSs) that are similar to what



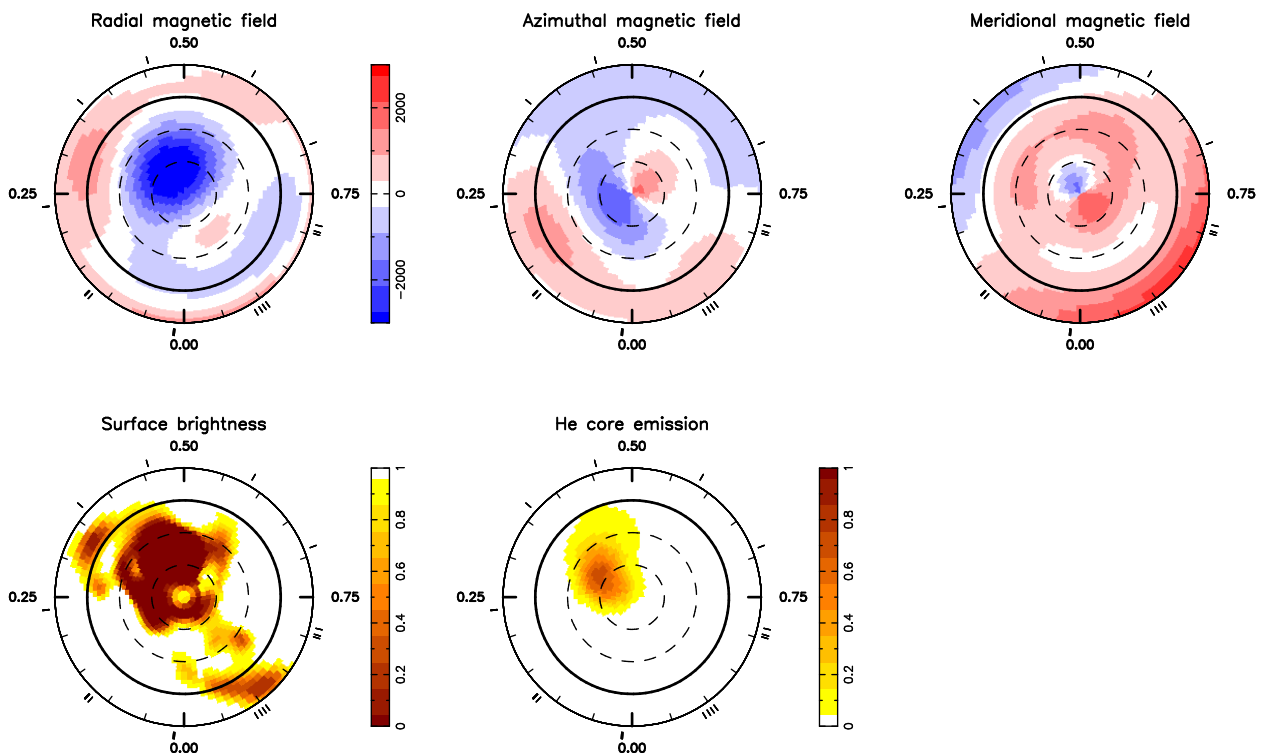


**Figure 5.** Reconstructed maps of the magnetic field (top left, middle and right panels for the radial, azimuthal and meridional components in spherical coordinates, all in G), relative photospheric brightness (bottom left) and accretion-induced He I emission in the NC (bottom right) at the surface of CI Tau, derived from the data set of Fig. 4 using tomographic imaging. The star is shown in a flattened polar projection down to a latitude of  $-30^\circ$ , with the north pole at the center and the equator shown as a bold line. Outer ticks depict phases of observations. Positive radial, azimuthal and meridional fields respectively point outwards, counterclockwise and polewards.

is observed on other cTTSs so far (e.g., Donati et al. 2011a, 2019), and phenomenologically consistent with what is expected from surface features being carried in and out of the observer’s view by rotation (e.g., Hébrard et al. 2014). We thus conclude that the observed 9-d modulation is unambiguously attributable to the rotation period of the star, and so are the photometric fluctuations at the same period that K2 revealed through continuous observations collected about 1–3 months after the end of our ESPaDOnS run (Biddle et al. 2018).

Using ZDI, we successfully modelled the parent large-scale magnetic field of CI Tau from the phase-resolved Zeeman signatures of both LSD photospheric and He I NC profiles. We find that CI Tau possesses a strong, mainly poloidal field, featuring a dipole component of about  $-1.7$  kG tilted at  $20^\circ$  with respect to the rotation axis, as well as a nearly aligned and parallel octupole field of similar strength, causing the radial field of CI Tau to peak at  $-3.7$  kG in a high-latitude region at phase 0.35. By simultaneously modelling the relative photospheric brightness and the accretion-induced NC of the He I  $D_3$  line, we show that the strong radial field region of CI Tau overlaps with a large dark spot at photospheric level and with a bright accretion region at chromospheric level, demonstrating that this area at the surface of the star is the main footpoint of magnetic accretion funnels linking the inner disc to the star. We note that the phase at which the dark spot is reconstructed in our photospheric brightness image (i.e., 0.35–0.40) agrees with that at which CI Tau is statistically faintest as measured from

the contemporaneous K2 photometry (once phased with our ephemeris, see Table 2), bringing still further support to the overall consistency of our tomographic modelling.

The magnetic field we reconstruct for CI Tau is consistent with the evolutionary stage and internal structure of the host star, i.e., intense and dominantly poloidal and axisymmetric as for all fully- and largely-convective cTTSs magnetically imaged to date (Gregory et al. 2012), and for all mature stars with masses in the range  $0.25$ – $0.50 M_\odot$  (Morin et al. 2008, 2010). We graphically summarize in Fig. 6 the magnetic properties of all cTTSs for which images are published in the literature, illustrating that all cTTSs more massive than  $0.4$ – $0.5 M_\odot$  and whose radiative envelope is thicker than about  $0.5 R_\star$  are apparently able to trigger strong poloidal and mainly axisymmetric fields, whereas the fully-convective ones of them tend to have most of the poloidal magnetic energy concentrating into the dipole field component.

Depending on the assumed value of the logarithmic mass accretion rate (with potential estimates ranging from  $-8.2$  for the He I NC, to  $-7.8$  and  $-7.7$  for H $\beta$  and H $\alpha$ , to  $-7.4$  for the He I BC, all in units of  $M_\odot \text{ yr}^{-1}$ , see Sec. 4), we infer that the radius  $r_{\text{mag}}$  of the magnetospheric cavity that CI Tau is able to carve at the centre of its accretion disc potentially ranges from  $6.3 R_\star$  down to  $3.7 R_\star$  (Bessolaz et al. 2008), or equivalently from  $0.72$  to  $0.42 r_{\text{cor}}$ . Taking the average value from the (unveiled) emission fluxes of H $\alpha$ , H $\beta$  and the He I BC (yielding a logarithmic mass accretion rate of  $-7.6 \pm 0.2$  in units of  $M_\odot \text{ yr}^{-1}$ ) as the most consistent es-

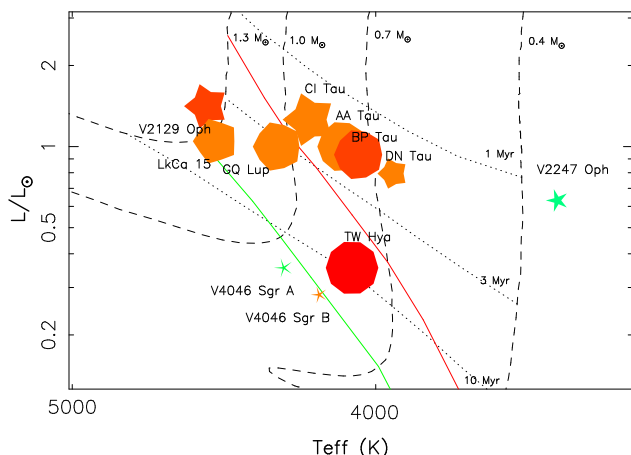


**Figure 6.** Main properties of the large-scale magnetic fields of cTTSs, as a function of their position in the HR diagram. Symbol size indicates relative magnetic fluxes, symbol color illustrates field configurations (red to blue for purely poloidal to purely toroidal fields), and symbol shape depicts the degree of axisymmetry of the poloidal field component (decagon and stars for purely axisymmetric and purely non-axisymmetric poloidal fields, respectively). The PMS evolutionary tracks and corresponding isochrones (Siess et al. 2000) assume solar metallicity and include convective overshooting. The full lines depict where models predict cTTSs start developing their radiative core (red line) and when their convective envelope gets shallower than  $0.5 R_{\star}$  (green line) as they contract towards the main sequence.

estimate, we find that  $r_{\text{mag}}$  barely extends half way to  $r_{\text{cor}}$ . In this context however, it is hard to understand how 85% of the accretion luminosity (i.e., the relative accretion luminosity associated with the He I BC with respect to that of both He I BC and NC) can be released before the accreted plasma even reaches the surface of the star; if the accretion luminosity that fuels the He I BC was indeed mostly released at the interface between the magnetosphere and the disc as suggested by Beristain et al. (2001) for stars like CI Tau, it should hardly exceed a small fraction of that associated with the He I NC for magnetospheric radii of a few  $R_{\star}$ , since at such distances, the kinetic energy stored in the Keplerian motion is much smaller than the potential energy that can be released through free fall (e.g., by factors of 6 and 14 at distances of 4 and 8  $R_{\star}$  respectively). Moreover, it is unclear whether poleward accretion could occur (as observed) from within  $0.5 r_{\text{cor}}$  given that the  $\ell = 1$  component of the field in the equatorial plane may not dominate the  $\ell = 3$  one by a large enough factor to efficiently deflect the accretion flow towards high latitudes at the stellar surface. Finally, we would unlikely witness ejection events in the form of narrow blue-shifted emission features like those we observe in Balmer lines (see Sec. 4 and Fig. 3 middle panels) if the inner disc penetrates so much within  $r_{\text{cor}}$ . We also note that accretion flows from  $0.5 r_{\text{cor}}$  would imply free-fall velocities of  $0.87 v_{\text{esc}}$ , smaller (though still marginally compatible) with velocities observed in the red wing of the 777.19 nm O I line reaching up to  $380 \text{ km s}^{-1}$  (i.e.,  $0.92 v_{\text{esc}}$ , see Sec. 4 and Fig. 3 right panel).

On the other hand,  $r_{\text{mag}}$  reaching out to  $0.8\text{--}1.0 r_{\text{cor}}$  for an average logarithmic mass accretion rate of  $-7.6 \pm 0.2$  (in units of  $M_{\odot} \text{ yr}^{-1}$ ) would require the dipole component of the

large-scale field to be  $2.4\text{--}3.6\times$  stronger than what we infer (i.e.,  $4.1\text{--}6.1 \text{ kG}$ ), which is not compatible with our spectropolarimetric data. The logarithmic mass accretion rate derived from the He I NC component only, equal to  $-8.2$  (in units of  $M_{\odot} \text{ yr}^{-1}$ ) and bringing  $r_{\text{mag}}$  within 30% of  $r_{\text{cor}}$ , i.e., in better agreement with some of the observed properties, is however most likely an underestimate in stars like CI Tau where the He I BC emission component dominates the NC, as pointed out by Beristain et al. (2001). We suspect that the actual mass accretion rate of CI Tau probably lies between the estimates inferred from the EWs of the He I NC and BC, with the latter being likely sensitive to a wider hot plasma environment than just the disc / magnetosphere interface and the accretion funnels in stars featuring intense accretion and dominant BC for most accretion proxies.

We stress again that our observations of CI Tau were collected at a time where accretion was unusually strong, i.e., with accretion luminosities derived from the He I BC and NC that are typically  $5\times$  larger than those inferred from Beristain et al. (2001). (In Beristain et al. 2001, the unveiled He I BC component of CI Tau is about as strong as the unveiled NC component in our data). Assuming the observations of Beristain et al. (2001) better represent the typical accretion status of CI Tau would imply that  $r_{\text{mag}}$  usually falls within  $0.7$  and  $1.0 r_{\text{cor}}$  (for accretion rates inferred from the EWs of the He I BC and NC respectively), i.e., close enough to  $r_{\text{cor}}$  for CI Tau to be in a situation of efficient spin-down through a propeller-like mechanism (Romanova et al. 2004; Ustyugova et al. 2006; Zanni & Ferreira 2013) and in agreement with its longer-than-average rotation period (of 9.0 d).

We also report that accretion on CI Tau is highly unsteady, with the (unveiled) EW of the He I BC (not modulated by rotation, see Sec. 4) fluctuating by as much as a factor of 2 in a stochastic way on a timescale of only a few days. This erratic behaviour also shows up through the rapid photometric changes observed during the continuous 80-d monitoring campaign of K2, even though rotational modulation at the 9-d period is still clearly visible in the light curve. This intrinsic variability likely reflects a very inhomogeneous density profile in the inner regions of the accretion disc.

More spectropolarimetric observations, in particular through campaigns monitoring the rotational modulation and stochastic variability of accretion proxies and photospheric lines at multiple epochs, are needed to constrain further the accretion geometry and magnetospheric properties of CI Tau, now that the rotation period of the star is well determined.

The 9-d modulation of photospheric lines, both in position and shape (as inferred from RVs and BSs, see Figs. 1 and 2), that results from the presence of brightness and magnetic features at the surface of CI Tau (in particular the large dark spot and magnetic region at phase 0.35), generates in our optical spectra RV fluctuations with a semi-amplitude of  $\approx 2 \text{ km s}^{-1}$  that are reminiscent of those reported by Johns-Krull et al. (2016), suggesting that they likely share the same origin. The obvious distortions in the shape of LSD profiles (see Fig. 4) and associated BS variations (see Fig. 2) clearly indicate that the RV modulation we

see on CI Tau is attributable to the activity jitter<sup>5</sup>, which is likely to show up at infrared wavelengths as well (with a different amplitude) given the strong magnetic fields detected at the surface of the star (Reiners et al. 2013).

Our result does not necessarily imply that the candidate close-in massive planet reported to orbit CI Tau (Johns-Krull et al. 2016) does not exist; in fact, given the apparently very active planet formation going on in the protoplanetary disc of this young star (Clarke et al. 2018), a hot Jupiter may indeed be present, orbiting at the outer boundary of the magnetospheric gap that almost extends out to the corotation radius. However, firmly demonstrating the existence of this putative hot Jupiter calls for definite evidence that is currently lacking, and that will likely be tricky to secure if the orbital period of the planet is indeed close to the rotation period of the star.

Recently, a CO signature, whose spectral location was reported to be modulated with the 9-d period and a semi-amplitude of  $77 \text{ km s}^{-1}$ , was detected in the spectrum of CI Tau and putatively attributed to the candidate planet's atmosphere (Flagg et al. 2019). The RV modulation of this CO signature points to a structure located at a distance of  $r_{\text{cor}}$  from the centre of the star (see Sec. 2), and crossing the line of sight when the dark photospheric spot is best visible (i.e., phase 0.4, see Sec. 5); an alternate option to tentatively account for the observed spectral signature is thus that CO is present in the inner disc regions near  $r_{\text{cor}}$ , with an azimuthal structure linked to the accretion funnels and reflecting the star-disc magnetic coupling. If confirmed, this would come as further evidence that the magnetosphere of CI Tau is at times able to extend as far as  $r_{\text{cor}}$ . Repeating such monitoring in spectropolarimetric mode, e.g., with an instrument like SPIrou (Donati et al. 2017a), now operational at CFHT, will allow one to quantify how this CO signature relates to the magnetosphere and to the large-scale field of the central star. More generally, surveying the modulation of CO lines in cTTSs may come up as a novel way to independently estimate  $r_{\text{mag}}$  (by directly measuring the distance at which accretion funnels merge with the inner disc), and thereby to improve our description and understanding of magnetospheric accretion processes in young forming stars.

Our study shows that CI Tau is an ideal laboratory to study the detailed physics of star-disc interactions in low-mass stars, in particular those hosting magnetic fields strong enough to be able to trigger, at least part of the time, ejection processes capable of efficiently spinning down the star through a propeller mechanism. This formation stage is indeed key for deciphering the early rotation history of Sun-like stars in the first few Myr of their life during which they vigorously interact with their discs (e.g., Gallet et al. 2019). That CI Tau is at the same time in a phase of active planet formation makes it even more interesting, for instance to find out whether it indeed hosts a massive planet that migrated close to the star after being formed further out in the disc. Multi-wavelength campaigns involving simultaneously optical and near-infrared high-resolution spectropolarimeters like SPIrou, capable of revealing through imaging tech-

niques what is occurring at the surface of the star, coupled to continuous precision photometry from space as obtained by K2 or TESS, is the key to such studies aimed at unveiling the origins of worlds like or unlike our Solar System.

## ACKNOWLEDGEMENTS

We thank an anonymous referee for valuable comments that enabled to clarify the analysis presented in this paper. Our study is based on data obtained at the CFHT, operated by the CNRC (Canada), INSU/CNRS (France) and the University of Hawaii. This project received funding from the European Research Council (ERC) under the H2020 research & innovation programme (grant agreements #740651 New-Worlds and #742095 SPIDI). SPHA acknowledges financial support from CNPq, CAPES and Fapemig. We also thank the Programme National de Physique Stellaire (PNPS) of CNRS/INSU for financial support. FM acknowledges funding from ANR of France under contract number ANR-16-CE31-0013.

## REFERENCES

- Andrews S. M., Rosenfeld K. A., Kraus A. L., Wilner D. J., 2013, *ApJ*, **771**, 129
- Beristain G., Edwards S., Kwan J., 2001, *ApJ*, **551**, 1037
- Bessolaz N., Zanni C., Ferreira J., Keppens R., Bouvier J., 2008, *A&A*, **478**, 155
- Biddle L. I., Johns-Krull C. M., Llama J., Prato L., Skiff B. A., 2018, *ApJ*, **853**, L34
- Bouvier J., Matt S. P., Mohanty S., Scholz A., Stassun K. G., Zanni C., 2014, *Protostars and Planets VI*, pp 433–450
- Brown S. F., Donati J.-F., Rees D. E., Semel M., 1991, *A&A*, **250**, 463
- Clarke C. J., et al., 2018, *ApJ*, **866**, L6
- David T. J., et al., 2016, *Nature*, **534**, 658
- Donati J.-F., 2003, in Trujillo-Bueno J., Sanchez Almeida J., eds, *Astronomical Society of the Pacific Conference Series Vol. 307*, Astronomical Society of the Pacific Conference Series. p. 41
- Donati J.-F., Brown S. F., 1997, *A&A*, **326**, 1135
- Donati J., Landstreet J. D., 2009, *ARA&A*, **47**, 333
- Donati J.-F., Semel M., Carter B. D., Rees D. E., Collier Cameron A., 1997, *MNRAS*, **291**, 658
- Donati J.-F., et al., 2006, *MNRAS*, **370**, 629
- Donati J.-F., et al., 2007, *MNRAS*, **380**, 1297
- Donati J., et al., 2010, *MNRAS*, **409**, 1347
- Donati J., et al., 2011a, *MNRAS*, **412**, 2454
- Donati J.-F., et al., 2011b, *MNRAS*, **417**, 472
- Donati J.-F., et al., 2012, *MNRAS*, **425**, 2948
- Donati J.-F., Kouach D., Lacombe M., Baratchart S., Doyon R., Delfosse X., et al. 2017a, SPIrou: A nIR Spectropolarimeter/High-precision Velocimeter for the CFHT. p. 107, doi:10.1007/978-3-319-30648-3\_107-1
- Donati J.-F., et al., 2017b, *MNRAS*, **465**, 3343
- Donati J. F., et al., 2019, *MNRAS*, **483**, L1
- Fang M., van Boekel R., Wang W., Carmona A., Sicilia-Aguilar A., Henning T., 2009, *A&A*, **504**, 461
- Flagg L., Johns-Krull C. M., Nofi L., Llama J., Prato L., Sullivan K., Jaffe D. T., Mace G., 2019, *ApJ*, **878**, L37
- Folsom C. P., et al., 2016, *MNRAS*, **457**, 580
- Gaia Collaboration 2018, VizieR Online Data Catalog, **1345**
- Gallet F., Zanni C., Amard L., 2019, arXiv e-prints, p. arXiv:1910.03995
- Galli P. A. B., et al., 2018, *ApJ*, **859**, 33

<sup>5</sup> The small reduction in the amplitude of the RV modulation between the blue and red regions of our spectra further supports this interpretation.

- Grankin K. N., Melnikov S. Y., Bouvier J., Herbst W., Shevchenko V. S., 2007, *A&A*, **461**, 183
- Gregory S. G., Donati J.-F., Morin J., Hussain G. A. J., Mayne N. J., Hillenbrand L. A., Jardine M., 2012, *ApJ*, **755**, 97
- Guilloteau S., Simon M., Piétu V., Di Folco E., Dutrey A., Prato L., Chapillon E., 2014, *A&A*, **567**, A117
- Gully-Santiago M. A., et al., 2017, *ApJ*, **836**, 200
- Hartigan P., Edwards S., Ghandour L., 1995, *ApJ*, **452**, 736
- Hartmann L., Herczeg G., Calvet N., 2016, *ARA&A*, **54**, 135
- Hébrard É. M., Donati J.-F., Delfosse X., Morin J., Boisse I., Moutou C., Hébrard G., 2014, *MNRAS*, **443**, 2599
- Hennebelle P., Teyssier R., 2008, *A&A*, **477**, 25
- Herczeg G. J., Hillenbrand L. A., 2014, *ApJ*, **786**, 97
- Johns-Krull C. M., Valenti J. A., Hatzes A. P., Kanaan A., 1999, *ApJ*, **510**, L41
- Johns-Krull C. M., et al., 2016, *ApJ*, **826**, 206
- Kenyon S. J., Hartmann L., 1995, *ApJS*, **101**, 117
- Lin D. N. C., Bodenheimer P., Richardson D. C., 1996, *Nature*, **380**, 606
- Morin J., et al., 2008, *MNRAS*, **390**, 567
- Morin J., Donati J., Petit P., Delfosse X., Forveille T., Jardine M. M., 2010, *MNRAS*, **407**, 2269
- Muto T., Machida M. N., Inutsuka S.-i., 2008, *ApJ*, **679**, 813
- Muzerolle J., Hartmann L., Calvet N., 1998, *AJ*, **116**, 455
- Pecaut M. J., Mamajek E. E., 2013, *ApJS*, **208**, 9
- Reiners A., Bean J. L., Huber K. F., Dreizler S., Seifahrt A., Czesla S., 2010, *ApJ*, **710**, 432
- Reiners A., Shulyak D., Anglada-Escudé G., Jeffers S. V., Morin J., Zechmeister M., Kochukhov O., Piskunov N., 2013, *A&A*, **552**, A103
- Romanova M. M., Ustyugova G. V., Koldoba A. V., Lovelace R. V. E., 2004, *ApJ*, **616**, L151
- Schiavon R. P., Batalha C., Barbuy B., 1995, *A&A*, **301**, 840
- Semel M., 1989, *A&A*, **225**, 456
- Siess L., Dufour E., Forestini M., 2000, *A&A*, **358**, 593
- Simon M., et al., 2017, *ApJ*, **844**, 158
- Simon M., et al., 2019, arXiv e-prints, p. [arXiv:1908.10952](https://arxiv.org/abs/1908.10952)
- Ustyugova G. V., Koldoba A. V., Romanova M. M., Lovelace R. V. E., 2006, *ApJ*, **646**, 304
- Vaytet N., Commerçon B., Masson J., González M., Chabrier G., 2018, *A&A*, **615**, A5
- Yu L., et al., 2017, *MNRAS*, **467**, 1342
- Zanni C., Ferreira J., 2013, *A&A*, **550**, A99

This paper has been typeset from a  $\text{\LaTeX}$  file prepared by the author.